Wide-voltage-window reversible control of electronic transport in electrolyte-gated epitaxial $BaSnO_3$

Helin Wang,[1] Jeff Walter,[1] Koustav Ganguly,[1] Biqiong Yu,[2] Guichuan Yu,[2] Zhan Zhang,[3] Hua Zhou,[3] Han Fu,[2,4] Martin Greven,[2] and Chris Leighton[1,*]

[1]*Department of Chemical Engineering and Materials Science, University of Minnesota, Minneapolis, Minnesota 55455, USA*
[2]*School of Physics and Astronomy, University of Minnesota, Minneapolis, Minnesota 55455, USA*
[3]*Advanced Photon Source, Argonne National Laboratory, Argonne, Illinois 60439, USA*
[4]*James Franck Institute, University of Chicago, Chicago, Illinois 60637, USA*

(Received 22 May 2019; published 2 July 2019)

The wide gap perovskite semiconductor $BaSnO_3$ has attracted much interest since the discovery of room temperature electron mobility up to $320\,cm^2\,V^{-1}\,s^{-1}$ in bulk crystals. Motivated by applications in oxide heterostructures, rapid progress has been made with $BaSnO_3$ films, although questions remain regarding transport mechanisms and mobility optimization. Here we report on a detailed study of epitaxial $BaSnO_3$ electric double layer transistors based on ion gel electrolytes, enabling wide-doping-range studies of transport in *single films*. The work spans an order of magnitude in initial n doping ($\sim 10^{19}$ to $10^{20}\,cm^{-3}$, with both oxygen vacancies and La), film thicknesses from 10–50 nm, and measurements of resistance, Hall effect, mobility, and magnetoresistance. In contrast with many oxides, electrolyte gating of $BaSnO_3$ is found to be essentially reversible over an exceptional gate voltage window (approaching ± 4 V), even at 300 K, supported by negligible structural modification in *operando* synchrotron x-ray diffraction. We propose that this occurs due to a special situation in $BaSnO_3$, where electrochemical gating via oxygen vacancies is severely limited by their low diffusivity. Wide-range reversible modulation of transport is thus achieved (in both electron accumulation and depletion modes), spanning strongly localized, weakly localized, and metallic regimes. Two-channel conduction analysis is then combined with self-consistent Schrödinger-Poisson and Thomas-Fermi modeling to extract accumulation layer electron densities and mobilities. Electrostatic electron densities approaching $10^{14}\,cm^{-2}$ are shown to increase room temperature mobility by up to a factor of ~ 24. These results lay the groundwork for future studies of electron-density-dependent phenomena in high mobility $BaSnO_3$, and significantly elucidate oxide electrolyte gating mechanisms.

DOI: 10.1103/PhysRevMaterials.3.075001

I. INTRODUCTION

The perovskite oxide semiconductor $BaSnO_3$ (BSO) has attracted substantial interest since the 2012 discovery of outstanding room temperature electron mobility [1–3]. The mobility (μ) reaches $320\,cm^2\,V^{-1}\,s^{-1}$ at a Hall electron density $n \approx 10^{20}\,cm^{-3}$ in La-doped bulk single crystals, the largest room temperature value among perovskite oxides [1]. Retention of high μ at this very high n also generates exceptional conductivity [4]. The outstanding mobility is thought to derive from relatively small electron effective mass (recently reported to be $\sim 0.2 m_e$, where m_e is the free electron mass [5,6]) in the dispersive Sn 5*s*-derived conduction band [7–9], as well as low electron-phonon scattering rate [4,8]. The high mobility, wide band gap (~ 3 eV), and high optical transparency [2] render BSO a candidate for several applications, including high mobility transistors, transparent electronics, power electronics, and as a component in complex oxide heterostructures. Recently, n doping of bulk crystals has also been demonstrated with rare-earth dopants (Nd and Pr, which are magnetic) and oxygen vacancies (V_O), going beyond La [10].

The potential for heterostructures and devices drives interest in BSO films, which, despite progress [1,2,4,11–16], have mobilities that lag bulk crystals. Electron doping with La (i.e., in $Ba_{1-x}La_xSnO_3$), Sb (i.e., in $BaSn_{1-x}Sb_xO_3$), and V_O (i.e., in $BaSnO_{3-\delta}$) have been employed in epitaxial BSO films grown by molecular beam epitaxy (MBE) [4,13,14,16], pulsed laser deposition (PLD) [1,2,12,15,17–19], and sputter deposition [11,20]. Peak 300 K mobilities with these methods reach $183\,cm^2\,V^{-1}\,s^{-1}$ (at $n = 1.3 \times 10^{20}\,cm^{-3}$) [14], $122\,cm^2\,V^{-1}\,s^{-1}$ (at $n = 1.1 \times 10^{20}\,cm^{-3}$) [15], and $22\,cm^2\,V^{-1}\,s^{-1}$ (at $n = 4 \times 10^{19}\,cm^{-3}$) [20], respectively. The suppressed μ relative to bulk, and the observation that it increases with doping to very high n ($\sim 10^{20}-10^{21}\,cm^{-3}$), have been interpreted to reflect high densities of charged defects in films [1,2,4,11,13,14,18,20,21]. In addition to ionized impurities [4], these include point defects that accommodate nonstoichiometry [4], dislocations from lattice mismatch [1,2,4,11,13,14,18,20–22], and Ruddlesden-Popper shear faults [14,23]. Dislocations are a particular problem as the 4.116 Å BSO lattice parameter is poorly matched to readily available perovskite substrates such as $SrTiO_3$, $PrScO_3$, etc. Dislocations are expected to be charged [1,2,4] in BSO, although the dislocation core structure and scattering potential are not well understood. Significantly, recent work has deconvoluted some of these scattering contributions via

*Corresponding author: leighton@umn.edu

their n dependence, improving understanding of mobility limiting factors [4]. Systematic control over n in BSO is thus very useful, both to better understand mobility limits and to study doping-dependent phenomena.

Naturally given the above, BSO-based field-effect transistors (FETs) have been fabricated, seeking not only to explore device potential, but also to electrostatically control n in single films, independent of chemical doping. BSO-based FETs with Al_2O_3, HfO_2, $LaInO_3$, $SrTiO_3$, and parylene dielectrics have been reported, yielding ON/OFF ratios up to 10^7 [24–28], sub-threshold swing of 0.65 V dec^{-1} [27], and field-effect μ up to 90 cm^2 V^{-1} s^{-1} [27]. While these are promising developments, from the perspective of fundamental studies of n-dependent transport such FETs are limited to $n \sim 10^{13}$ cm^{-2} ($\sim 10^{19}$ cm^{-3}) [26], modest compared to chemical doping limits in BSO. Other approaches are thus being explored, including ferroelectric gating of BSO (potentially increasing n) [29], and polarization doping in heterostructures such as $LaInO_3/BaSnO_3$ [30,31].

A complementary approach, now established as highly effective in wide-range modulation of carrier density in oxides (and indeed more broadly), is electrolyte gating in electric double layer transistors (EDLTs) [32,33]. In this approach, the dielectric in a FET is replaced with an electrolyte, often an ionic liquid or ion gel. The latter are simply ionic liquids in polymer networks, generating easily processed solid electrolytes with high ionic mobility [33,34]. When a gate voltage (V_g) is applied in an oxide EDLT (positive, for example), cations in the ionic liquid or gel are driven to the surface of the oxide, which they typically cannot penetrate, leading to accumulation. Charge is then balanced by accumulation of electrons on the oxide side of the interface, forming an electric double layer (EDL). The primary advantage of the EDLT is that, in a simple picture, the EDL is a parallel plate capacitor with thickness $\sim$1 Debye length, generating very large capacitances, up to 100 μF/cm^2 [32,33]. These translate to electrostatically accumulated carrier densities up to $10^{14}-10^{15}$ cm^{-2} at V_g within the electrochemical stability window of typical ionic liquids (a few volts), one to two orders-of-magnitude beyond conventional FETs [32]. These densities are large enough, in fact, to induce electronic phase transitions [32]. In oxides alone this has enabled electrical control over zero temperature (T) insulator-metal transitions (IMTs) [32,35], T-dependent IMTs [32,36,37], Mott IMTs [32,36], superconductivity [32,38–40], and magnetic order and properties [41–44].

In 2017, Fujiwara *et al.* [45] applied ionic liquid gating to nominally undoped PLD-grown epitaxial BSO films and achieved n up to 2×10^{14} cm^{-2} at $V_g = +6$ V. This was sufficient to induce an IMT in films thicker than 100 nm, and substantially raise mobility, which was found to scale as $\mu \sim n^{3/2}$ before decreasing at the highest n [45]. Mobilities of 220 and 300 cm^2 V^{-1} s^{-1} were obtained at 150 and 50 K, respectively [45], comparable to the best reported in BSO films. While such results are highly encouraging, they also raise questions. For example, data were not obtained by Fujiwara *et al.* at room temperature, above the freezing point of the ionic liquid, due to high gate current (I_g). Metallicity could also only be induced at high BSO thickness (above $\sim$105 nm), and a H_2O etch was required to generate sufficiently smooth surfaces. Moreover, gate biases of +6 V are very large for ionic liquid EDLTs, and reversibility after bias removal was not reported. The latter point is important, as it is now understood that electrolyte gate response in EDLTs can be not only electrostatic, but also *electrochemical* [46]. In oxides, V_O can be created by the EDL electric field, for example, resulting in V_g-controlled electrochemical doping, as detected from transport irreversibility [47,48], studies in O_2 vs inert atmospheres [47,49–51], and *operando* probes such as x-ray diffraction [52–54] and absorption spectroscopy [54,55]. V_O-based electrochemical response has been thus detected in many oxides, including VO_2 [49], TiO_2 [51], $SrTiO_3$ [50], $SrRuO_3$ [43], $NdNiO_3$ [54,56], $La_{0.5}Sr_{0.5}CoO_{3-\delta}$ [47,53], and $YBa_2Cu_3O_{7-x}$ [55]. H^+ ions created by hydrolysis of H_2O contaminants can also be electrochemically doped into oxides in EDLTs, as in WO_3 [57,58], $SrCoO_{2.5}$ [41], and VO_2 [59,60]. Although in their infancy, efforts are underway to understand when and why electrochemical vs electrostatic response occurs in oxide EDLTs [46]. Such mechanistic understanding is lacking for BSO, meaning that full appreciation of the potential and limitations of BSO EDLTs has not yet been achieved.

Here we report on a detailed study of ion-gel-gated, smooth, epitaxial BSO films grown by high pressure oxygen sputter deposition. Expanding substantially on prior BSO EDLT work, a range of initial chemical doping is explored (from $n \approx 10^{19}-10^{20}$ cm^{-3}, achieved via La and V_O doping), in films of thickness $d = 10-50$ nm. In contrast to many oxides, largely reversible modulation of transport is found over an exceptional V_g range (approaching $\pm$4 V), even at 300 K, *in vacuo*. *Operando* synchrotron x-ray diffraction further confirms that no detectable structural changes occur vs V_g. This remarkable reversibility is ascribed to a special situation in BSO: the vacancy formation enthalpy is low, meaning that V_O can form, but their diffusivity is also extremely low, rendering them essentially immobile. Any electrochemical gate response due to V_O is therefore confined to the extreme surface of BSO, rendering it practically indistinguishable from ideal, reversible, electrostatic response. Wide-range modulation of transport is thus explored vs initial doping level, in both accumulation and depletion modes, spanning strongly localized to metallic regimes. In particular, a crossover from variable range hopping to weak localization is electrically tuned, tracked via resistance and magnetoresistance. The important case of electron accumulation at positive V_g is then analyzed in detail, using two-channel conduction analysis with self-consistent Schrödinger-Poisson and Thomas-Fermi modeling to extract accumulation layer electron densities and mobilities. Induced electron densities approaching 10^{14} cm^{-2} are shown to improve room temperature mobility by up to a factor of $\sim$24, reaching 51.4 cm^2 V^{-1} s^{-1} in sputtered films. These results lay the groundwork for future studies of n-dependent transport in high mobility BSO films, also shedding new light on oxide electrolyte gating mechanisms.

II. EXPERIMENTAL METHODS

Conditions for high pressure oxygen sputter deposition of undoped BSO were reported in our prior work [11]. Briefly, rf sputtering at 65–75 W from a nominally stoichiometric

2 in. ceramic BSO target was performed in 1.5 Torr of ultrahigh-purity O_2, on to a 750 °C substrate [11]. As-grown films were then vacuum annealed at 900 °C for 4 h at $<10^{-7}$ Torr to controllably V_O dope [11,20]. The resultant room temperature n increases with d, from $\sim 1 \times 10^{19}\,\mathrm{cm}^{-3}$ at 10 nm to $\sim 5 \times 10^{19}\,\mathrm{cm}^{-3}$ at 50 nm. This is ascribed to increased densities of compensating defects near the substrate interface, and to possible surface/interface depletion effects [11,20]. The resultant room temperature μ ranges from 0.5 to $22\,\mathrm{cm}^2\,\mathrm{V}^{-1}\,\mathrm{s}^{-1}$. To explore a wider range of initial chemical doping, which was not studied in prior BSO EDLT work [45], 50-nm-thick La-doped BSO films were also grown, via dc high pressure oxygen sputtering. A nominally stoichiometric 2 in. ceramic $La_{0.02}Ba_{0.98}SnO_3$ target was dc sputtered at ~45 W in 1.9 Torr of ultrahigh-purity O_2, onto 850 °C substrates. The La-doped BSO films used here have $n \approx 1 \times 10^{20}\,\mathrm{cm}^{-3}$ and $\mu \approx 30\,\mathrm{cm}^2\,\mathrm{V}^{-1}\,\mathrm{s}^{-1}$ at 300 K. Note that in all cases in this work, $LaAlO_3$(001) substrates were used. While this generates large mismatch (−8.6%) it eliminates the possibility of annealing- or gate-induced V_O in the substrate ($LaAlO_3$ does not readily form V_O), removing a source of erroneous results. All films are thus relaxed. As will be reported in a future publication [61], this choice of substrate has surprisingly little impact on μ. Detailed structural and chemical characterization of high pressure oxygen sputtered BSO was provided previously [11]. For illustration, we report here high-resolution wide-angle x-ray diffraction (WAXRD) and grazing-incidence x-ray reflectivity (GIXR) data, acquired on a Panalytical X'Pert using Cu K_α radiation. Contact mode atomic force microscopy (AFM) data from a Bruker Nanoscope V Multimode 8 system are also shown.

EDLT fabrication employed similar methods to our prior work on other oxides [42,47]. As shown in the top- and side-view schematics in Figs. 1(a) and 1(b), $1 \times 1\,\mathrm{mm}^2$ BSO channels were defined by Ar ion milling, with a steel mask. Ti(20 nm)/Au(60 nm) gate and channel electrodes were then sputtered using a second steel mask, and a four-wire van der Pauw geometry was employed for channel resistance measurement. Note that Ti-induced reduction of the BSO may occur under the contact region, but that this will only serve to improve ohmicity and lower the contact resistance. "Cut and stick" ion gels [34] consisting of 80 wt. % ionic liquid [1-ethyl-3-methylimidazolium bis(trifluoromethylsulfonyl)amide ([EMI][TFSI])] in 20 wt. % polymer [poly(vinylidene fluoride-*co*-hexafluoropropylene) (P(VDF-HFP))] were then applied to form EDLTs. As shown in Fig. 1(a), three sections of gel were applied, one covering the BSO channel, the others ensuring high areal coverage of the gate electrodes. Immediately after application of the gel, devices were transferred to a Quantum Design Inc. Physical Property Measurement System (PPMS) for T-dependent transport measurements from 2–300 K in magnetic fields to 9 T, or to a closed-cycle refrigerator where 300 K V_g response was measured in vacuum ($<10^{-4}$ Torr). dc excitation was employed to measure channel resistance, using a Keithley 220 current source and Keitheley 2002 voltmeter. V_g and I_g were applied and measured using a Keithley 2400 source-measure unit. Following work on electrolyte-gated $La_{0.5}Sr_{0.5}CoO_{3-\delta}$ [53], *operando* structural characterization under V_g was also

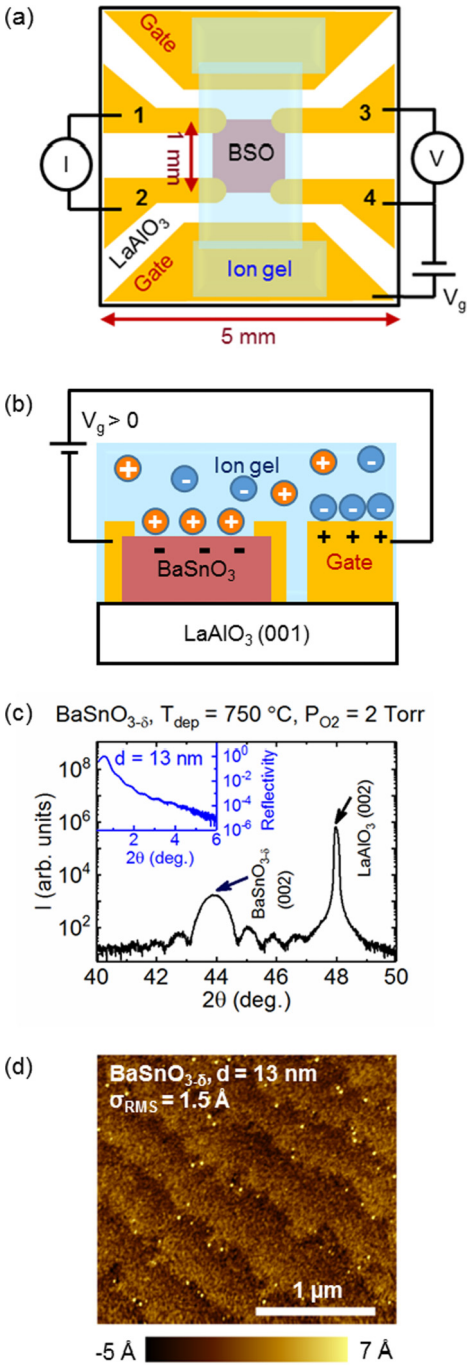

FIG. 1. Device schematics; structural characterization of $BaSnO_{3-\delta}$ epitaxial films. Top view (a) and side view (b) schematics of $BaSnO_3$ electric double layer transistors. Shown are the $5 \times 5\,\mathrm{mm}^2$ $LaAlO_3$(001) substrate (white), $1 \times 1\,\mathrm{mm}^2$ $BaSnO_3$ (BSO) channel (red), Ti/Au electrodes (gold color), and the ion gel (pale blue). Electrodes 1–4 are for van der Pauw measurement, while the others are gate electrodes. I, V, and V_g are the injected current, measured voltage, and gate voltage, respectively. Orange and blue circles depict gel cations and anions, while the +/− depict holes/electrons. (c) High-resolution wide angle x-ray diffraction (around the 002 film and substrate reflections) from a $LaAlO_3$(001)/$BaSnO_{3-\delta}$ film of thickness $d = 13$ nm. Inset: Grazing-incidence x-ray reflectivity from the same film. (d) Contact mode atomic force microscopy image of the same film, revealing root-mean-square roughness $\sigma_{RMS} = 1.5$ Å.

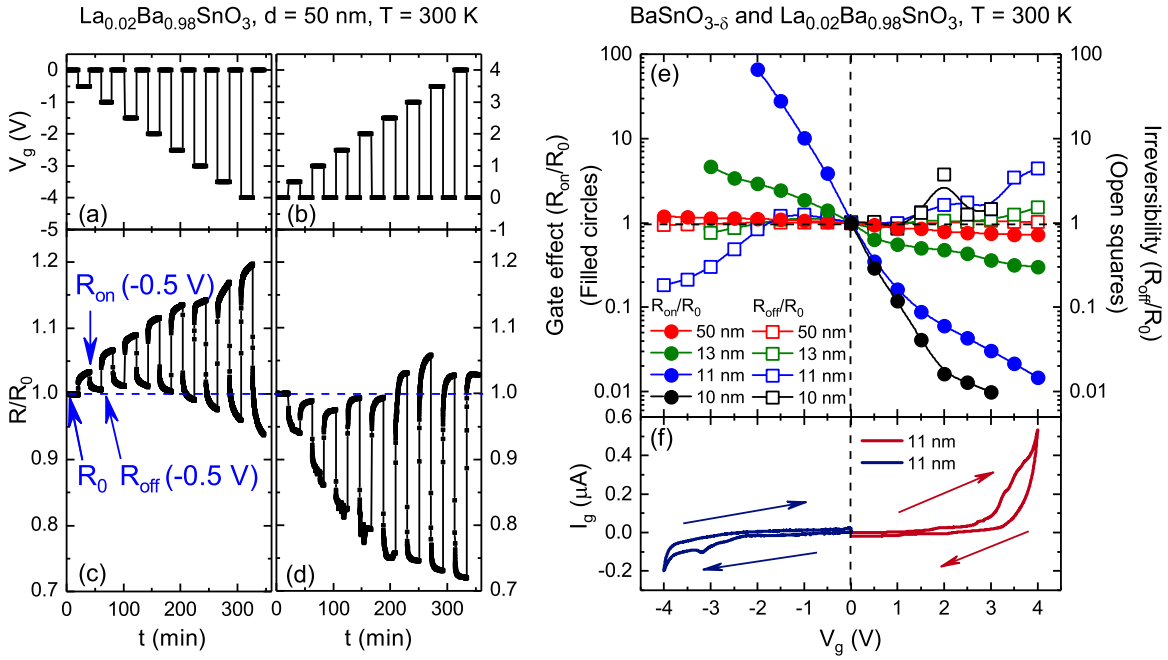

FIG. 2. 300 K gate effect and reversibility of ion-gel-gated $Ba_{1-x}La_xSnO_{3-\delta}$ films. (a) and (b) Negative and positive gate voltage (V_g) vs time (t) square wave sequences (20 min periods) applied to a device based on 50-nm-thick $LaAlO_3(001)/La_{0.02}Ba_{0.98}SnO_3$. (c) and (d) Corresponding sheet resistance (R) vs t, plotted as R/R_0 where R_0 (horizontal blue dashed line) is $R(t = 0)$. Also illustrated are definitions of R_{on} and R_{off} (using 0.5 V as an example), i.e., the resistance at the end of a 20 min V_g pulse, and 20 min after V_g removal. (e) V_g dependence of the gate effect (R_{on}/R_0, filled circles) and irreversibility (R_{off}/R_0, open squares) for devices based on 50-nm-thick $LaAlO_3(001)/La_{0.02}Ba_{0.98}SnO_3$ (red) and $LaAlO_3(001)/BaSnO_{3-\delta}$ of thickness 13 (green), 11 (blue), and 10 nm (black). Solid lines are guides to the eye connecting points. At 10 nm thickness, data could not be acquired at negative V_g due to the high magnitude of R and/or gate current I_g. (f) Corresponding I_g vs V_g for a device based on 11-nm-thick $LaAlO_3(001)/BaSnO_{3-\delta}$. Red: V_g sweep from 0 to 4 to 0 V. Blue: V_g sweep from 0 to −4 to 0 V. Sweep rates were 5 mV/s and arrows indicate directions.

performed, via synchrotron x-ray diffraction (SXRD) on the 33-ID beamline of the Advanced Photon Source, Argonne National Laboratory, with 20 keV ($\lambda = 0.62$ Å) radiation. Those measurements were made in vacuum ($<10^{-5}$ Torr), with each V_g applied at 300 K for ∼30 min, and SXRD scans being taken in the last ∼6 min. As discussed in Supplemental Material Section A (Fig. S1) [62], at $V_g = 0$, at least ∼8 scans (i.e., ∼50 min of exposure) were possible before detectable beam damage, sufficient to obtain the data presented here.

III. RESULTS AND DISCUSSION

A. Structural characterization

As noted above, detailed structural and chemical characterization of high pressure oxygen sputtered BSO was provided earlier [11]. Illustrative of the films studied here, Figure 1(c) shows high-resolution specular WAXRD from a $d = 13$ nm $LaAlO_3(001)/BaSnO_{3-\delta}$ film. Only the 002 film and substrate peaks appear, as expected, in-plane grazing incidence diffraction confirming cube-on-cube epitaxy [11]. The out-of-plane lattice parameter from Fig. 1(c) is 4.123 Å, consistent with our prior work, with the expansion over bulk ascribed to defects rather than residual strain [11]. Finite size fringes around the BSO 002 peak indicate low surface roughness, as does the observation of Kiessig fringes to ∼5° in GIXR [inset to Fig. 1(c)]. This is corroborated by contact-mode AFM images of the same film [Fig. 1(d)], which show root-mean-square roughness of 1.5 Å over $2.5 \times 2.5\,\mu m^2$, along with terraces between unit-cell-high steps. Some evidence of decoration of the surface with particles is seen, which could result from surface contamination or BaO [45,63].

B. Electrolyte gating mechanism

As in prior work on ion-gel-gated $La_{0.5}Sr_{0.5}CoO_{3-\delta}$ [47], *in vacuo* response of the channel sheet resistance (R) to application and removal of V_g was used to assess reversibility and elucidate mechanisms. Figures 2(c) and 2(d) show example data for a $d = 50$ nm La-doped BSO film, measured at $<10^{-4}$ Torr and 300 K. This film had initial $n = 8.0 \times 10^{19}$ cm^{-3} and $\mu = 29.9$ cm^2 V^{-1} s^{-1}. Gate voltages of increasing magnitude (up to ±4 V in 0.5 V steps) were applied and removed on a 20 min cycle, with both negative [Fig. 2(a)] and positive [Fig. 2(b)] polarities. Resultant $R(t)$ traces (t = time) for negative and positive V_g are shown in Figs. 2(c) and 2(d), respectively, normalized to R_0, the $t = 0$ value of R.

Beginning at negative V_g, Fig. 2(c) first shows that R remains stable at R_0 for the first 20 min, during which $V_g = 0$. In contrast to electrolyte-gated $La_{0.5}Sr_{0.5}CoO_{3-\delta}$ [47], and other oxides [40], transport in these BSO EDLTs is thus stable after application of the ion gel, even at 300 K. In $La_{0.5}Sr_{0.5}CoO_{3-\delta}$ this is only possible below ∼260 K; above this R drifts upward with t, ascribed to electrochemical

reduction of the film surface even at $V_g = 0$ [47]. This is a first indication of the relative electrochemical stability of BSO EDLTs. Application of $V_g = -0.5$ V in Fig. 2(c) then induces a sharp increase in R, followed by a gradual increase over 20 min, reaching $R_{on}(-0.5\text{ V})/R_0$ of 1.034. The resistance change is positive, consistent with electrostatic depletion of electrons in this initially chemically n-doped film. When V_g is returned to zero, R decreases quickly initially, then more slowly, reaching $R_{off}(-0.5\text{ V})/R_0$ of 1.006 after 20 min. This is close to 1, i.e., almost fully reversible. The remainder of Fig. 2(c) illustrates how R_{on} and R_{off} evolve at larger magnitudes of negative V_g, out to -4 V. While long time scale effects are present, and R_{off}/R_0 begins to dip below 1 at the highest $|V_g|$, the gating is remarkably reversible. Note that a significant contributor to the relatively sluggish $R(t)$ is the side-gate geometry [Figs. 1(a) and 1(b), used here to enable *operando* SXRD], which separates the channel and gates by mm distances [47,53]. Figure 2(d) reveals similar characteristics for $V_g > 0$. Long time scale effects are visible, but with only modest irreversibility (i.e., small deviations from $R_{off}/R_0 = 1$), even at large V_g. The sign is also as expected, the decrease in R being consistent with electron accumulation.

The data of Figs. 2(c) and 2(d) are summarized in Fig. 2(e) by plotting the 300 K V_g dependence of the gate effect (defined as R_{on}/R_0) and irreversibility (defined as R_{off}/R_0), on $\log_{10}$ scales. With the latter definition, $R_{off}/R_0 = 1$ corresponds to ideally reversible behavior. For a broader view, Fig. 2(e) shows these ratios not only for the $d = 50$ nm La-doped BSO film from Figs. 2(c) and 2(d), but also three additional V_O-doped BSO films, with $d = 10$, 11, and 13 nm. Initial 300 K n and μ values thus span from 1.7×10^{19} cm^{-3} and 0.5 cm^2 V^{-1} s^{-1} ($d = 10$ nm, V_O doped) to 8.0×10^{19} cm^{-3} and 29.9 cm^2 V^{-1} s^{-1} ($d = 50$ nm, La doped). Considering the gate effect first (solid symbols, left axis), the polarities of response are as expected in each film, R_{on}/R_0 going above 1 at negative V_g (depletion), and below 1 at positive V_g (accumulation). A stronger gate effect is also observed on going from the 50-nm-thick La-doped film to the 13-nm-thick V_O-doped film, to the 10-nm-thick V_O-doped film, consistent with the lower initial n and d. The gate effect at $d = 11$ nm in fact reaches almost four orders-of-magnitude between -2 and $+4$ V, achieved here at 300 K. For the $d = 10$ nm V_O-doped film, the initial R(300 K) becomes so large ($\sim$4 MΩ/sq) that data at $V_g < 0$ (i.e., in depletion) could not be recorded.

In terms of irreversibility (open points, right axis), the main observation is the relatively small deviations from $R_{off}/R_0 = 1$, which are barely visible for the La-doped and $d = 13$ nm V_O-doped films. Some irreversibility does arise in the 11-nm-thick V_O-doped film, but at $V_g = +4$ V, where a two order-of-magnitude gate effect occurs, this is only a factor of $\sim$4. Similarly, at $V_g = -2$ V, where a gate effect of the opposite polarity of two orders-of-magnitude occurs, the irreversibility is negligible. We thus conclude that the gate effects here are predominantly reversible, even at 300 K, and over a ± 4 V range, independent of initial chemical doping. Moreover, the limited irreversibility that does arise at large V_g magnitudes can also be shown to be associated with the ion gel, *not* the BSO. Working with $d = 11$ nm V_O-doped films, for example, V_g of ± 4 V was applied for 20 min, V_g returned to zero, the ion gel removed, and the BSO film surface cleaned. The latter was achieved by sonication in acetone, followed by baking in vacuum at 100 °C. As shown in Supplemental Material Section B (Fig. S2) [62], R returns to within 50% of its initial value after this process, and the BSO can be regated with a new ion gel, demonstrating that the film is not irreversibly damaged. We thus ascribe what limited irreversibility occurs in Fig. 2 to electrochemical degradation of the ion gel, rather than the BSO.

The above picture is further supported by Fig. 2(f) which plots the V_g dependence (to ± 4 V, both ascending and descending V_g) of I_g for the $d = 11$ nm V_O-doped BSO film in Fig. 2(e). The data are largely devoid of the peaks that would indicate distinct electrochemical processes [41,64] (except perhaps at -3.25 V, see below), and are instead dominated by only gradual onset of significant $|I_g|$ at the highest $|V_g|$. In these devices, with 1 mm^2 channels, $|I_g|$ in fact only exceeds 0.1 μA at $V_g < -3.15$ V and $V_g > 3.04$ V. We ascribe this current to electrochemical degradation at the very highest V_g, mostly of the gel, but potentially also involving residual H_2O [41]; the small potential peak at -3.25 V is likely of the same origin. More specifically, electrochemical consumption of cations (anions) in the gel at the BSO surface at positive (negative) V_g would lead to interfacial anion (cation) excess after removal of V_g, resulting in R_{off} being larger (smaller) than R_0, as observed in Fig. 2(e). Similar phenomena may also explain the small peak in irreversibility around $V_g = 2$V in Fig. 2(e); hydrolysis of residual H_2O could lead to excess hydroxide ions at the BSO surface and thus $R_{off} > R_0$. This $\sim$2 V irreversibility peak could not be eliminated even by 3 h of *in situ* 130 °C annealing at 10^{-3} Torr, potentially due to the known difficulty of removing residual water [41]. As a final comment on Fig. 2(f), we note that the $|I_g|$ recorded here at 300 K are certainly sufficiently low to enable reliable V_g- and T-dependent BSO transport studies. We are thus not restricted to low T [45].

Further support for unusual reversibility over an exceptional V_g window is provided by *operando* SXRD. Figures 3(a) and 3(b) show 300 K specular SXRD data collected around the 002 film and substrate reflections for an ion-gel-gated $d = 13$ nm V_O-doped BSO film at $V_g = 0, -1, -2, -3$ V [Fig. 3(a)] and $V_g = 0, +1, +2, +3, +4$ V [Fig. 3(b)]. The $V_g = 0$ BSO 002 peak occurs at $L = 1.839$ [the L axis is in substrate reciprocal lattice units (r.l.u.)], corresponding to an out-of-plane lattice parameter of 4.125 Å, consistent with Fig. 1(c). The striking feature at nonzero V_g is the almost complete absence of changes with gating. Some evidence of a barely detectable decrease in the amplitude of BSO Laue fringes may arise at $V_g = -3$ and $+4$ V, but could also be due to minor beam damage. Aside from this, the BSO Bragg peak position, peak width, and fringe structure are essentially V_g independent. Note here that *in situ* transport measurements were performed on the beamline during SXRD data acquisition (Supplemental Material Section A [62]) confirming that gating did take place. As a point of comparison, gate-induced V_O formation in an electrochemically active material such as $La_{0.5}Sr_{0.5}CoO_{3-\delta}$ leads to very large (1%) out-of-plane lattice parameter expansion at V_g of only $+2$ V, accompanied by strong damping of Laue oscillations [53],

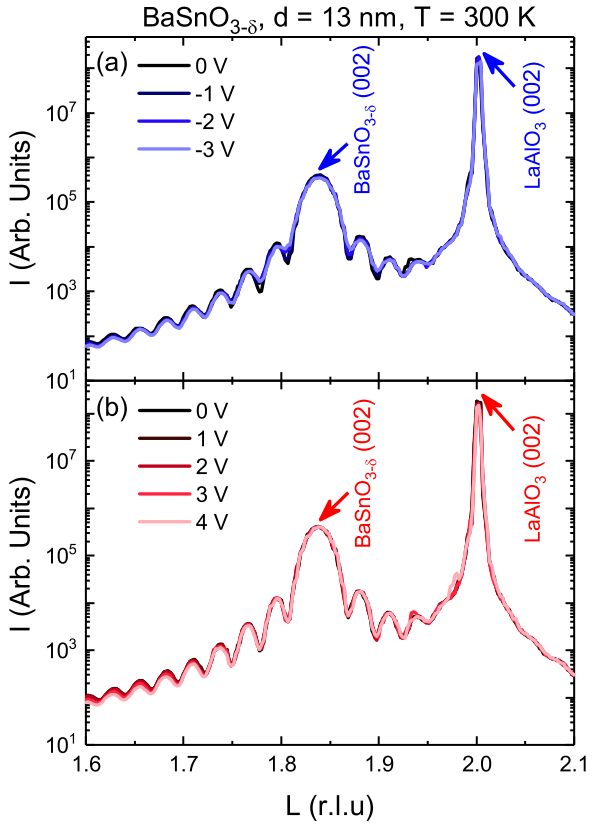

FIG. 3. *Operando* synchrotron x-ray diffraction on ion-gel-gated $BaSnO_{3-\delta}$ films. Specular $00L$ scans (around the 002 film and substrate reflections) from 13-nm-thick $LaAlO_3(001)/BaSnO_{3-\delta}$ films at (a) $V_g \leqslant 0$, and (b) $V_g \geqslant 0$. *Substrate* reciprocal lattice units (r.l.u) are used.

i.e., substantial and obvious changes in *operando* SXRD. The data in Fig. 3 are thus remarkably V_g independent.

Together, Figs. 2 and 3 provide compelling evidence of unusually reversible electrolyte-gate response in BSO, over an exceptional V_g window (approaching ± 4 V), accompanied by negligible structural modifications, even at 300 K *in vacuo*. Electrochemical response via V_O formation thus appears negligible, in contrast to many oxides. Importantly, this cannot be explained in terms of the V_O formation enthalpy ΔH_{Vo}. The latter may be ~ 1 eV in BSO [20], comparable to $SrTiO_3$ [65], for example, where electrochemical response via V_O in ionic liquid EDLTs is known to be large [50]. Also, other oxides that exhibit V_O formation under electrolyte gating, such as VO_2, are known to have quite large ΔH_{Vo} [49], suggesting that there is no clear link between V_O formation in electrolyte gating and ΔH_{Vo} alone. What is dramatically different in BSO, however, in comparison for example to other cubic perovskite oxide semiconductors such as $SrTiO_3$, is the V_O *diffusivity*. In BSO this has been reported to be $D_{Vo} \approx 10^{-16}\,cm^2\,s^{-1}$ at $\sim 500\,^\circ C$ [66], extremely low in comparison to the 10^{-7}–$10^{-6}\,cm^2\,s^{-1}$ in many other perovskite oxides at this temperature [67]. In fact, assuming a typical ΔE of ~ 1 eV in $D = D_0\ \exp(-\Delta E/k_B T)$, where k_B is Boltmann's constant, an extrapolated D_{Vo} as low as $\sim 10^{-27}\,cm^2\,s^{-1}$ is predicted at 300 K in BSO. As noted in the BSO literature [10,66], these are exceptionally low D_{Vo}, so low, in fact, that post-growth reduction (as used in this work to V_O dope) is effective only in thin films, not bulk single crystals [10]. V_O still occurs in the latter, but their density is locked-in during growth [10]. The result of this situation is that under the gating conditions used here (300 K, 20 min) the BSO V_O diffusion length, $l = (Dt)^{1/2} < 1$ Å. Any V_O that do form under V_g are therefore confined to the extreme surface region of the BSO. We propose that this special situation is the origin of the strikingly reversible, wide-V_g-window behavior seen here at 300 K in BSO EDLTs, and also recently in $SrSnO_3$ EDLTs [68]. Electrochemical effects due to V_O are strongly suppressed by the exceptionally low V_O diffusivity, meaning that redox response, if present, is essentially indistinguishable from ideal electrostatic accumulation and depletion of electrons. With this insight, future work studying electrochemical vs. electrostatic response in electrolyte-gated oxides with systematically varied ΔH_{Vo} and D_{Vo} would clearly be worthwhile. With regard to gating mechanisms involving H^+, liberated by potential hydrolysis from residual H_2O, we emphasize that the very long time scale effects and large R_{off}/R_0 characteristic of electrolyte-induced H^+ doping [41,57–60] are absent here.

C. Temperature-dependent transport

Armed with understanding of the mechanisms of electrolyte gating in BSO EDLTs, we now progress to discussion of T-dependent transport. Shown in Fig. 4 are $R(T)$ plots at multiple V_g [Figs. 4(a), 4(d), and 4(g)], along with the V_g dependence of the apparent 2D Hall electron density n_H^{2D} [Figs. 4(c), 4(f), and 4(i)] and mobility μ_H [Figs. 4(b), 4(e), and 4(h)], at $T = 2$, 150, and 300 K. Data are shown for three films: $d = 50$ nm La-doped BSO (top panel), $d = 12$ nm V_O-doped BSO (middle panel), and $d = 10$ nm V_O-doped BSO (bottom panel), with systematically decreasing initial 3D Hall density (n_0^{3D}) and mobility (μ_0), as given in the figure. It should be emphasized here that $n_H^{2D}(V_g)$ and $\mu_H(V_g)$ in these plots are *apparent* values, directly extracted from Hall data, not accounting for current shunting due to the doped BSO region under the accumulation/depletion layer at the interface with the ion gel. The further analysis required for us to determine electrostatic doping depth profiles, and thus more quantitatively understand such data, is provided in Sec. III D.

Starting with the $d = 50$ nm La-doped BSO film with $n_0^{3D} = 8.0 \times 10^{19}\,cm^{-3}$ and $\mu_0 = 29.9\,cm^2\,V^{-1}\,s^{-1}$, Fig. 4(a) shows typical $V_g = 0$ behavior at such relatively heavy initial doping. [Note that *two* $V_g = 0$ curves are shown in Fig. 4(a), for reasons explained in the caption]. R first decreases on cooling from 300 K (metallicklike behavior) before presenting an upturn below ~ 50 K; such behavior will be shown below to be due to weak localization. Application of $V_g = \pm 4$ V (i.e., electron accumulation/depletion) then results in modulation of low T resistance by -32 and $+39\%$, respectively, the relatively modest changes being due to the high thickness and initial chemical doping. The only change in the form of $R(T)$ is weakening of the low T upturn at lower R, i.e., at positive V_g. Weakly localized transport is thus apparent at all V_g in Fig. 4(a), approaching positive dR/dT at all T at the highest accumulated electron densities, where R is $\sim 1\%$ of h/e^2 [i.e., 26 kΩ (h = Planck's constant, e = electronic charge)]. We

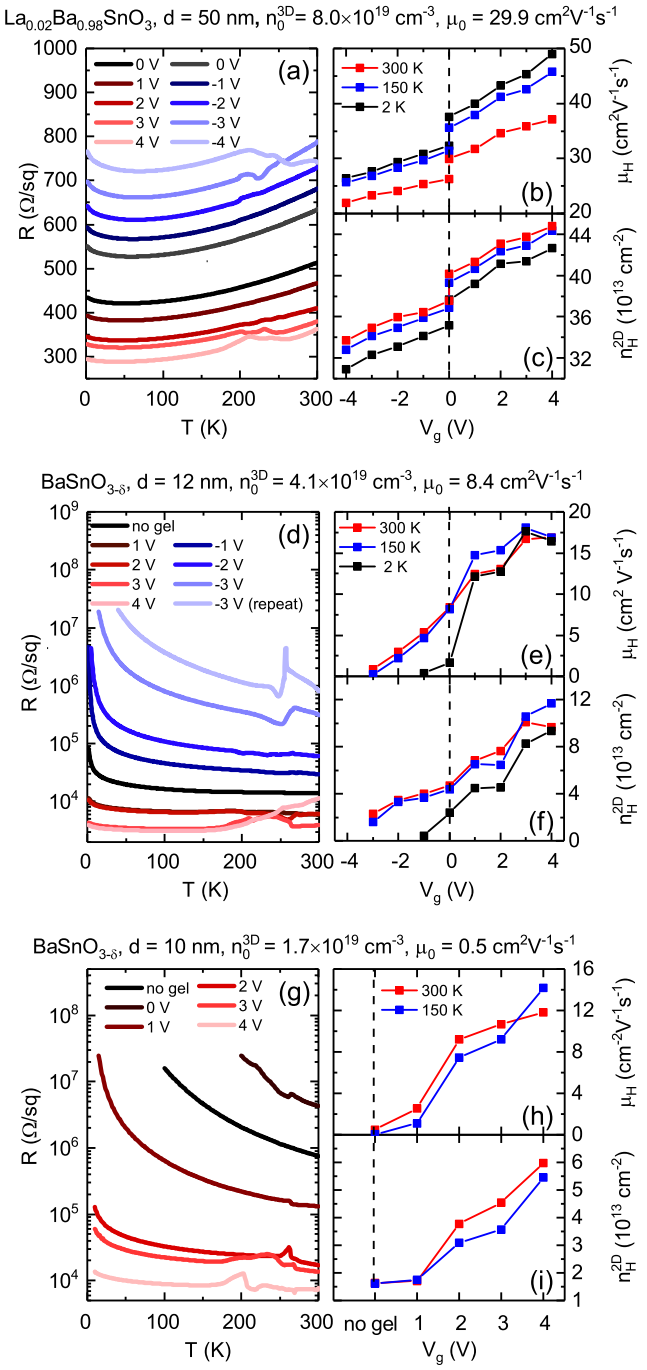

FIG. 4. Temperature- and gate-voltage-dependent transport in $Ba_{1-x}La_xSnO_{3-\delta}$ films. Temperature (T) dependence of the sheet resistance (R) at various V_g for (a) 50-nm-thick $LaAlO_3(001)/La_{0.02}Ba_{0.98}SnO_3$, (d) 12-nm-thick $LaAlO_3(001)/BaSnO_{3-\delta}$, and (g) 10-nm-thick $LaAlO_3(001)/BaSnO_{3-\delta}$. (b) and (c), (e) and (f), and (h) and (i) show corresponding V_g dependences of the apparent Hall mobility μ_H and 2D Hall electron density n_H^{2D} at 300, 150, and 2 K for the same films. The labels above the panels indicate the film type, thickness (d), and initial 3D Hall electron density n_0^{3D} and Hall mobility μ_0. In (h) and (i), 2 K data could not be collected due to the large resistances. Note that in (a)–(c) *two* sets of data are shown at $V_g = 0$. In this particular device, positive V_g was applied first, exploring magnitudes as large as 6 V. Some shift in R was thus found on returning to $V_g = 0$ and performing measurements at negative V_g.

note parenthetically here that the irregular features in $R(T)$ in the 200–300 K range are associated with the freezing point of the ionic liquid, and are common in EDLTs [35,69]. As shown in Figs. 4(b) and 4(c), n_H^{2D} and μ_H evolve qualitatively as expected with V_g and T. Specifically, at 300 K, n_H^{2D} increases by 12% with V_g up to +4 V, consistent with additional electron accumulation, whereas n_H^{2D} decreases by 10% with V_g down to −4 V, consistent with depletion. Again, the relatively small V_g-induced changes in n_H^{2D} are due to the high thickness and initial chemical doping, which render electrostatic effects modest. The resulting μ_H increases monotonically from −4 to +4 V, consistent with the typical increase in μ with n in BSO films [20], due to screening of charged defects. Moving to T dependence, $n_H^{2D}(T)$ is seen to be weak [Fig. 4(c)], consistent with the expected degenerate doping at these doping levels [11,20]. μ_H, on the other hand, increases by as much as 26% on cooling from 300 to 2 K at $V_g = 0$, indicative of significant electron-phonon scattering at these relatively high μ [11,20].

The $d = 12$ nm V_O-doped film (middle panel) with $n_0^{3D} = 4.1 \times 10^{19}\,\mathrm{cm}^{-3}$ and correspondingly lower $\mu_0 = 8.4\,\mathrm{cm}^2\,\mathrm{V}^{-1}\,\mathrm{s}^{-1}$ shows significantly different behavior. R(300 K) at $V_g = 0$ is ∼30 times higher than in the 50 nm La-doped case, $R(T)$ showing a ∼10-fold increase on cooling to 2 K. The initial state is thus significantly more insulating, consistent with the lower n_0^{3D}. Electron depletion at V_g down to −3 V then results in strongly localized transport, shown in Sec. III E to be due to variable-range hopping. Conversely, electron accumulation at V_g up to +4 V results in rather flat $R(T)$ with $R < h/e^2$ (26 kΩ). As detailed in Sec. III E, this device thus presents an apparent strong- to weak-localization crossover, spanning well over four orders-of-magnitude in low T resistance. As shown in Figs. 4(e) and 4(f), the corresponding behaviors of n_H^{2D} and μ_H are qualitatively as expected. The gate-induced modulation of n_H^{2D} is much stronger than in the $d = 50$ nm La-doped BSO device, due to the lower initial doping. n_H^{2D} in fact becomes unmeasurable at the largest negative V_g and lowest T due to high R; related to this, in Fig. 4(f) at low T and −1 V, hopping conduction likely makes μ_H somewhat unreliable. Consistent with the lower initial doping, even at the highest accumulated electron densities μ_H reaches only $\sim 18\,\mathrm{cm}^2\,\mathrm{V}^{-1}\,\mathrm{s}^{-1}$, with no increase on cooling, indicative of dominant defect scattering [20].

Finally, the $d = 10$ nm V_O-doped BSO film, with $n_0^{3D} = 1.7 \times 10^{19}\,\mathrm{cm}^{-3}$ and $\mu_0 = 0.5\,\mathrm{cm}^2\,\mathrm{V}^{-1}\,\mathrm{s}^{-1}$ shows yet different behavior. $R(T)$ before ion gel application in this case is already strongly insulating, R exceeding 10^7 Ω at ∼100 K. This is consistent with the expected high defect density at low d in highly lattice-mismatched BSO, which will generate compensation, trapping, strong scattering, and surface/interface depletion. As noted in the discussion of Fig. 2(e), the electrostatic depletion regime can thus not be studied in such devices due to very high R. Application of positive V_g up to 4 V results in $R < 10^4$ Ω, however, accompanied by weak $R(T)$, meaning that a crossover from strongly localized to weakly localized/metallic transport remains possible at low n_0^{3D}. This is consistent with the study of Fujiwara *et al.* [45] on nominally undoped BSO, although very thick films (100s of nm), and gate biases up to +6 V (potentially beyond the electrochemical stability window of the ionic liquids [33,70]) were required to achieve metallicity in that work. One

other notable feature in Fig. 4(g), found only in such highly insulating films, is the non-negligible effect of ion gel application even at $V_g = 0$. At 300 K, R increases by a factor of ~6 after gel application, likely indicating ion-gel-induced doping even at $V_g = 0$. This is not uncommon in EDLTs [32,33,71], and can derive from preferential association of one ion type with the semiconductor surface, amplified here by the strong $\mu(n)$. Moving on to Figs. 4(h) and 4(i), n_H^{2D} and μ_H are now easily interpreted due to the low thickness and highly insulating starting BSO. Under these conditions the accumulation layer at positive V_g essentially carries all of the current. The induced electron density reaches 6×10^{13} cm^{-2}, within a factor of 2 of Fujiwara *et al.* [45], and in the typical range for *semiconducting* EDLTs [32,33]. Significantly, μ_H at 300 K is increased from 0.5 to 11.9 cm^2 V^{-1} s^{-1} (i.e., a factor of 24) by this interfacial electron accumulation, as discussed below. As already noted, however, extracting accurate corresponding $\mu(n)$ from heavier doped, thicker, films [as in Figs. 4(a)–4(f)] requires knowledge of the depth profile of the accumulated electron density.

D. Quantitative analysis of electrostatic doping profiles and accumulation layer parameters

Extraction of estimated accumulation layer electron densities and mobilities from the V_g-dependent data discussed above was achieved by modeling the depth profile of electrostatic doping and applying a two-channel conduction model. In this manner, transport parameters in the accumulation layer near the interface with the ion gel at positive V_g can be separated from those of the underlying BSO, even in the presence of initial chemical doping. In the absence of known $\mu(n)$, models featuring continuous variation of n and μ with depth (z) are not feasible [72], and so a discrete two-channel parallel conduction model was applied. In such a model [72,73],

$$n_H^{2D}\mu_H = n_A^{3D}\mu_A d_A + n_B^{3D}\mu_B d_B, \tag{1}$$

$$n_H^{2D}\mu_H^2 = n_A^{3D}\mu_A^2 d_A + n_B^{3D}\mu_B^2 d_B, \tag{2}$$

where n_H^{2D} and μ_H are the apparent Hall electron density and mobility (as shown in Fig. 4), n_A^{3D} and μ_A are the 3D carrier density and mobility in the accumulation layer, and n_B^{3D} and μ_B are the 3D carrier density and mobility in the "bulk" region, under the accumulation layer. This bulk region is considered to have identical properties to starting films, i.e., $n_B^{3D} = n_0^{3D}$ and $\mu_B = \mu_0$. In addition, the thicknesses of the accumulation and bulk layers obey $d_A + d_B = d$. Extraction of n_A^{3D} and μ_A from the data shown in Fig. 4 (as well as n_A^{2D}) then only requires estimation of d_A, which we define as the thickness of the region in which 90% of the electrostatically induced electrons are confined.

To fully understand the induced carrier depth profile, and accurately determine d_A, both Thomas-Fermi (TF) approximation [74] and self-consistent Schrödinger-Poisson (SP) numerical modeling [75] was performed. A full description is provided in Supplemental Material Section C (including Fig. S3) [62]. Briefly, the TF approximation treats electrons in the accumulation layer as a 3D free electron gas, which is appropriate when $k_F d_A \gg 1$, where $k_F = (3\pi^2 n_A^{3D})^{1/3}$ is the Fermi wave vector [74]. TF calculations were performed by solving the Poisson equation,

$$\frac{d^2\varphi(z)}{dz^2} = -\frac{4\pi\rho_c(z)}{\varepsilon_r}, \tag{3}$$

where $\varphi(z)$ is the potential profile, $\rho_c(z)$ is the charge density profile, and ε_r is the relative permittivity. In the TF approximation [74] this is supplemented with the relation

$$e\varphi(z) = (3\pi^2)^{2/3}\frac{\hbar^2}{2m_e^*}[n^{3D}(z)]^{2/3}, \tag{4}$$

where m_e^* is the electron effective mass. Combining Eqs. (3) and (4) with standard boundary conditions then enables numerical computation of $n^{3D}(z)$ and $\varphi(z)$. More accurate SP modeling, on the other hand, treats the accumulation layer electrons as a 2D quantum mechanical gas confined in the potential well created by V_g at the BSO/ion gel interface. This is done by self-consistently solving Eq. (3) with the Schrödinger equation. For a 2D electron gas in the effective mass approximation this reduces to solving a 1D Schrödinger equation for an envelope function $\psi(z)$ [75],

$$-\frac{\hbar^2}{2m_e^*}\frac{d^2\psi(z)}{dz^2} + [-e\varphi(z) - E]\psi(z) = 0. \tag{5}$$

The charge density $\rho_c(z)$ is then expressed as a sum of the electron density in each band:

$$\rho_c(z) = e\left\{n_d^+ - \beta k_B T\sum_i |\psi_i(z)|^2 \times \ln\left[1 + \exp\left(-\frac{E_i - E_F}{k_B T}\right)\right]\right\}, \tag{6}$$

where n_d^+ is the density of ionized donors, E_F is the Fermi energy, $\beta = \frac{m_e^*}{\pi\hbar^2}$, k_B is Boltzmann's constant, and ψ_i and E_i are the normalized envelope wave function and eigenenergy of the ith state [75]. Self-consistent calculations then proceed by numerically solving (5) using the TF method as an initial input, then inputting the result into (6). The Poisson equation (3) is then solved and the process repeated until convergence is achieved. Details are provided in Supplemental Material Section C [62]. Note that while the SP method is implemented here at 300 K, and TF is a $T = 0$ theory, for the degenerately doped films studied here the SP results are very similar at 0 and 300 K.

V_g-dependent electrostatically-induced electron distributions [$n^{3D}(z)$] calculated via these TF (blue curves) and SP methods (red curves) are shown in Fig. 5(a) for an illustrative $d = 50$ nm La-doped BSO film. Here $z = 0$ is placed at the substrate/BSO interface, so that $z = 50$ nm corresponds to the BSO/ion gel interface. The qualitative features in Fig. 5(a) are essentially as expected. The two approaches agree in the tail of the $n^{3D}(z)$ distribution (approaching 8×10^{19} cm^{-3}, the initial chemical doping level), but differ at the BSO/ion gel interface. In the latter limit the TF approach yields a V_g-dependent constant at $z = 50$ nm, inherent to a boundary condition in the model (see Supplemental Material Section C [62]), whereas the SP calculations yield $n^{3D} \to 0$ as the ion gel is entered. A peak in $n^{3D}(z)$ thus forms in the SP data, in this case at ~1 nm from the interface, but of course shifting towards

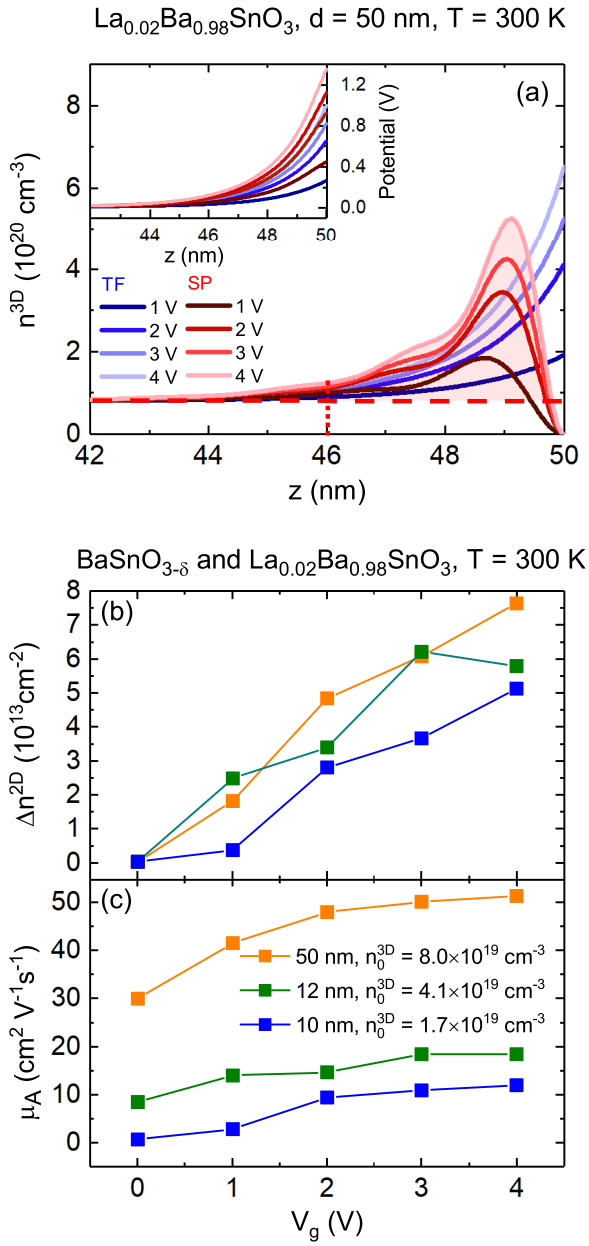

FIG. 5. Two-channel analysis and accumulation layer calculations for ion-gel-gated $Ba_{1-x}La_xSnO_{3-\delta}$ films. (a) 3D charge carrier density n^{3D} vs depth z in 50-nm-thick $LaAlO_3(001)/La_{0.02}Ba_{0.98}SnO_3$ at various V_g, calculated using the Thomas-Fermi (TF) approach (blue shades) and the self-consistent Schrodinger-Poisson (SP) approach (red shades). The $La_{0.02}Ba_{0.98}SnO_3$/ion gel interface is at $z = 50$ nm. The red shaded area indicates 90% of the induced electron density at $V_g = 4$ V, which is confined within 4 nm (vertical red dotted line) of the interface. The horizontal red dashed line marks n^{3D} at $V_g = 0$. Inset: Corresponding electrostatic potential vs z. (b) and (c) V_g dependence of the induced 2D electron density Δn^{2D} and accumulation layer mobility μ_A extracted via the SP approach for the three devices in Fig. 4 (50-nm-thick $LaAlO_3(001)/La_{0.02}Ba_{0.98}SnO_3$, 12-nm-thick $LaAlO_3(001)/BaSnO_{3-\delta}$, 10-nm-thick $LaAlO_3(001)/BaSnO_{3-\delta}$ films).

the interface with increasing V_g [76]. Importantly, however, with both methods, ~90% of the electrostatically induced electrons reside in a ~4-nm-thick channel (vertical red dotted line) at the BSO/ion gel interface, only weakly dependent on V_g. Accurate values for d_A can thus be confidently determined for use in Eqs. (1) and (2). We note that for $d_A \approx 4$ nm, the condition for validity of the TF approximation can be checked. It can be seen that $k_F d_A > 1$ when $n_A^{3D} \geqslant 5.3 \times 10^{17}\,\mathrm{cm}^{-3}$; the TF approximation is thus applicable for all BSO films in this work, where $n_A^{3D} \geqslant n_0^{3D} \geqslant 1.7 \times 10^{19}\,\mathrm{cm}^{-3}$. For completeness, shown in the inset to Fig. 5(a) are the accompanying V_g-dependent potential profiles $\varphi(z)$, which are set to zero deep in the film. Similar shapes are obtained from the TF and SP methods, but with generally lower magnitudes from TF modeling [76]. Although our devices have gate area much larger than channel area, to maximize potential drop at the critical interface, the interface ($z = 50$ nm) potentials are nevertheless lower than the applied V_g. This indicates that the experimentally obtained electron densities are lower than those predicted by simple modeling. This is because these models ignore significant factors such as traps, localized states, and electrochemistry, and rely on the effective mass approximation and so on. We note that the TF method, despite its simplicity, is able to capture the main features of the electron density and potential profile, providing a good estimate of d_A and $\varphi(z)$.

Calculations of this type were repeated for all films in this study, to determine d_A values. Equations (1) and (2) were then applied to the data shown in Fig. 4 to extract n_A^{3D} (and thus n_A^{2D}) and μ_A. Figures 5(b) and 5(c) summarize the results by plotting the 300 K accumulation-mode V_g dependence of the induced 2D electron density, Δn^{2D} [Fig. 5(b)] and μ_A [Fig. 5(c)]. Δn^{2D} is similar for all three films shown, reaching almost $8 \times 10^{13}\,\mathrm{cm}^{-2}$ at $V_g = +4\,V$. This is similar to reported values in many ionic-liquid- or ion-gel-gated inorganic and organic semiconductors [32,33], and within a factor of ~2 of the Fujiwara *et al.* BSO EDLT result [45]. The latter was obtained at +6 V, however, and in our case we achieved this with demonstrated reversibility. Figure 5(b) also shows slightly reduced Δn^{2D} as the initial chemical doping n_0^{3D} is decreased (e.g., in the $d = 10$ nm V_O-doped case), which we ascribe to a lower accessible density of extended states, and higher trap density.

The corresponding $\mu_A(V_g)$ behavior in Fig. 5(c) reveals substantial increases in mobility with electron accumulation in all cases. The $d = 50$ nm La-doped BSO device with initial mobility of $29.9\,\mathrm{cm}^2\,\mathrm{V}^{-1}\,\mathrm{s}^{-1}$ is increased to $51.4\,\mathrm{cm}^2\,\mathrm{V}^{-1}\,\mathrm{s}^{-1}$ (a 72% increase), while the $d = 12$ nm V_O-doped BSO with initial mobility $8.4\,\mathrm{cm}^2\,\mathrm{V}^{-1}\,\mathrm{s}^{-1}$ is increased to $18.4\,\mathrm{cm}^2\,\mathrm{V}^{-1}\,\mathrm{s}^{-1}$ (a 120% increase). This mobility boost is consistent with the general increase in μ with n seen in BSO, due to improved screening of charged defects, particularly dislocations [1,2,4,13,20]. Ion gel gating enables this without increasing the ionized impurity density, however. A future study is planned to examine $\mu_A(n)$ in this manner in even higher quality MBE-grown films with larger μ_0 [77]. We note for now, however, that the as-deposited La-doped BSO and peak gated mobilities reported here (29.9 and $51.4\,\mathrm{cm}^2\,\mathrm{V}^{-1}\,\mathrm{s}^{-1}$, respectively), are outstanding for sputtered BSO. The factor of 24 improvement from 0.5 to $11.9\,\mathrm{cm}^2\,\mathrm{V}^{-1}\,\mathrm{s}^{-1}$ in the $d = 10$ nm BSO EDLT is also noteworthy. The initial mobility in such films is suppressed by strong disorder and compensation due to the low d (particularly due to misfit dislocations

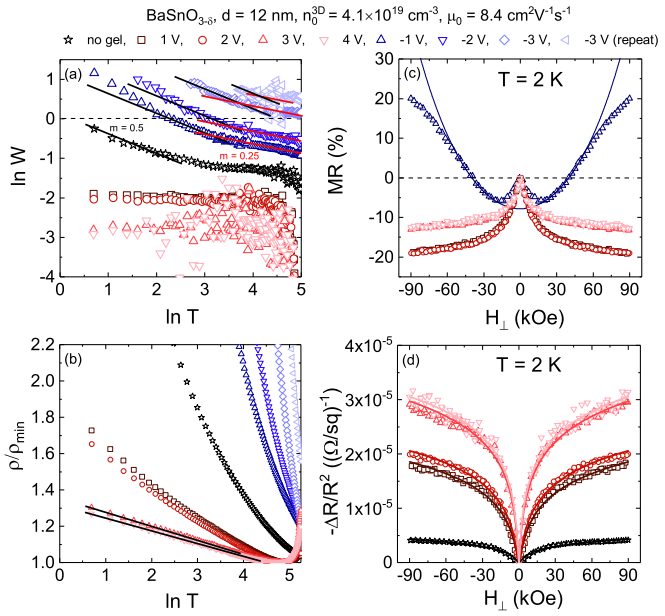

FIG. 6. Temperature-dependent resistivity and magnetoresistance in ion-gel-gated 12-nm-thick $LaAlO_3(001)/BaSnO_{3-\delta}$. (a) $\ln W$ vs $\ln T$ at various V_g, where $W = -d\ln(\rho)/d\ln(T)$, yielding the exponent m in $\rho = \rho_0 \exp(T_0/T)^m$ as the slope. Black and red solid lines show $m = 0.5$ and 0.25. (b) ρ/ρ_{min} vs $\ln T$ at various V_g, where ρ_{min} is the minimum resistivity. Black solid lines are straight line fits. (c) and (d) 2 K perpendicular magnetic field ($H_\perp$) dependence of the magnetoresistance [$MR = [(\rho(H_\perp) - \rho(0))/\rho(0)]\times 100\%$] (c) and $\Delta R/R^2$ (where R is sheet resistance) (d), at various V_g. The solid line in (c) is a fit to a variable-range hopping model described in the text. Solid lines in (d) are fits to a 2D weak localization model yielding Thouless lengths l_{Th} of 80–140 nm, as described in the text. The V_g legend at the top applies to all panels.

[22,23]). As discussed in the next section, such mobility increases are very likely driven by strong to weak localization crossovers, i.e., from hopping conduction to weakly localized transport.

E. Gate-tuned strong to weak localization crossover

To illustrate the power of electrolyte gating for wide-range manipulation of electronic transport in single BSO films we now focus in more depth on the $d = 12$ nm V_O-doped film with $n_0^{3D} = 4.1 \times 10^{19}$ cm^{-3} and $\mu_0 = 8.4$ cm^2 V^{-1} s^{-1}. The data of Fig. 4(d) suggest the possibility of a strong to weak localization crossover in this film, which we now show is supported by more detailed analysis (Fig. 6). The V_g-dependent $R(T)$ data of Fig. 4(d) are first replotted in Fig. 6(a) on a Zabrodskii plot [78], i.e., as $\ln W$ vs $\ln T$, where $W = -d\ln(\rho)/d\ln(T)$ and $\rho = Rd$ is the apparent resistivity. Such plots are used to linearize the form

$$\rho = \rho_0 \exp(T_0/T)^m, \tag{7}$$

where ρ_0 and T_0 are constants, as is typically observed at low T deep on the insulating side of the IMT. An exponent $m = 1$ indicates simple activated behavior or nearest-neighbor hopping, while $m = 0.5$ indicates Efros-Shklovskii variable-range hopping (ES VRH), and $m = 0.25$ indicates 3D Mott variable-range hopping (Mott VRH), for example [79–81].

As shown in Fig. 6(a), this initial BSO film, and all negative V_g curves (i.e., electron depletion), present approximately straight lines with negative slope in the low T limit on this Zabrodskii plot, indicating some form of exponential T dependence. As indicated by the black solid lines, $m = 0.5$ is supported from 0 to -3 V, setting in at some V_g-dependent T between $\sim$70 and 10 K. The widest ranges of adherence to $m = 0.5$ (at $V_g = -1$, -2 V) reach one order-of-magnitude in T and almost two orders-of-magnitude in ρ. Extracted T_0^{ES} values range from 370 to 40 K, and the T-dependent VRH activation energies safely exceed the lowest measurement temperature at $V_g < -1$ V. We thus conclude that ES VRH is active at low T between 0 and -3 V [82]. As is often the case, however, ES VRH gives way to a weaker T dependence at higher T [79,83,84], in this case with $m = 0.25$ [red solid lines in Fig. 6(a)]. This indicates a crossover to Mott VRH [79,83,84]. This is supported by analysis of the scaling between T_0^{ES} and T_0^{Mott}, which follows the expected relation, as shown in Supplemental Material Section D, Fig. S4 [62]. As also shown in Fig. 6(a), positive V_g (i.e., electron accumulation) results in very different behavior: $\ln W$ becomes negative, the slope of $\ln W$ vs $\ln T$ becoming small before inverting to positive slope at the highest V_g. This indicates a reduced activation energy that *decreases* on cooling, i.e., nonexponential, metalliclike behavior [78]. As illustrated in Fig. 6(b), which plots ρ/ρ_{min} vs $\ln T$ where ρ_{min} is the minimum resistivity, at the largest positive V_g the weak increase in ρ on cooling in fact becomes logarithmic over a reasonably wide T interval (2 to $\sim$90 K). This is consistent with conductance $G(T) \propto \ln(T/T_0')$, where T_0' is a constant, characteristic of both weak localization and electron-electron interaction quantum corrections in 2D [81].

To further clarify the origin of this crossover from exponential (ES VRH) to logarithmic T dependence, low T perpendicular field magnetoresistance (MR) data were taken and analyzed. $MR = [(\rho(H_\perp) - \rho(0))/\rho(0)] \times 100\%$ is plotted vs perpendicular (out-of-plane) field $H_\perp$ in Fig. 6(c), at 2 K, for all V_g at which 2 K measurements were possible (-1 to $+4$ V). At -1 V, where Fig. 6(a) shows positive $\ln W$ at low T and clear ES VRH, $MR(H_\perp)$ is clearly dominated by a positive component. As shown by the blue solid line, the positive MR component is of the form

$$\ln\left(\frac{R}{R(H_\perp = 0)}\right) = \frac{se^2}{\hbar^2} L_c^4 H_\perp^2 \left(\frac{T_0^{ES}}{T}\right)^{3/2}, \tag{8}$$

where $s = 0.0015$, and L_c is the electron localization length. This is as expected for ES VRH, where perpendicular fields reduce wave function overlap, generating positive MR [79], the deviations at high field being ascribable to factors such as other MR contributions, weak-to strong-field limits, minor self-heating, etc. The extracted localization length in this case is 11 nm. The negative MR component at low field then grows with electron accumulation, V_g from 0 to $+4$ V resulting in sign reversal to entirely negative MR, characteristic of the field-induced dephasing effect in weak localization [79,81]. Quantitatively confirming this, Fig. 6(d) shows the 0 to $+4$ V MR data replotted as $-\Delta R/R^2$ vs $H_\perp$, along with fits (solid

lines) to

$$\frac{-\Delta R}{R^2} = \frac{e^2}{2\pi^2\hbar}\left[\Psi\left(\frac{1}{2}+\frac{\hbar/2e}{l_{el}l_{in}H_\perp}\right) - \ln\left(\frac{\hbar/2e}{l_{el}l_{in}H_\perp}\right)\right], \quad (9)$$

where Ψ is the digamma function, and l_{el} and l_{in} are the elastic and inelastic scattering lengths [79,81]. This expression for weak-localization-driven negative perpendicular field MR (i.e., positive magnetoconductance) is seen to describe the data well, yielding Thouless lengths $l_{Th} = \frac{1}{2}\sqrt{l_{el}l_{in}}$ that increase from 80 to 140 nm with electron accumulation. Importantly, in all cases $l_{Th} \gg d$, consistent with 2D weak localization. The analysis in Fig. 6 thus provides compelling evidence of a gate-tuned strong to weak localization crossover, highlighting the utility of electrolyte gating for wide-range modulation of the electronic properties and ground state in BSO.

IV. SUMMARY

In conclusion, ion gel gating of thoroughly characterized epitaxial $BaSnO_3$ thin films has been shown to enable wide-range modulation of electron density, resistance, and mobility, studied vs film thickness and initial chemical doping level. Gate-voltage-dependent measurements of *in vacuo* irreversibility, gate current, and structure (from *operando* synchrotron x-ray diffraction) reveal a remarkable level of reversibility, even at 300 K. We argue that this occurs due to a special situation in $BaSnO_3$, where oxygen vacancy diffusion is so slow that electrochemical electrolyte gate response is strongly suppressed, resulting in behavior indistinguishable from simple electrostatic accumulation and depletion of electrons. Calculations of depth profiles of electrostatic doping were then used in conjunction with two-channel conduction modeling to extract accumulation layer electron densities and mobilities, even in the presence of initial chemical doping. Strong enhancement of mobility with electron accumulation is deduced, reaching a factor of 24 and resulting in peak room temperature mobility of 51.4 $cm^2\,V^{-1}\,s^{-1}$ in sputtered $LaAlO_3(001)/La_{0.02}Ba_{0.98}SnO_3(50\,nm)$ films. Finally, a gate-tuned crossover from strong to weak localization has been established, verified by detailed analysis of temperature- and magnetic-field-dependent transport. These results shed important new light on oxide electrochemical gating mechanisms in general, in addition to paving the way for future electron-density-dependent studies of high mobility $BaSnO_3$ thin films.

ACKNOWLEDGMENTS

Work supported by the National Science Foundation through the UMN MRSEC under Grant No. DMR-1420013. Parts of this work were performed in the Characterization Facility, UMN, which receives partial support from NSF through the MSREC program. Portions of this work were conducted in the Minnesota Nano Center, which is supported by the NSF through the national Nano Coordinated Infrastructure Network, Award Number NNCI-1542202. Part of this work also used resources of the Advanced Photon Source, a DOE Office of Science user facility operated by Argonne National Laboratory under DE-AC02-06CH11357. We gratefully acknowledge B. Shklovskii, K. Reich, and B. Jalan for useful discussions.

[1] H. J. Kim, U. Kim, H. M. Kim, T. H. Kim, H. S. Mun, B. G. Jeon, K. T. Hong, W. J. Lee, C. Ju, K. H. Kim, and K. Char, Appl. Phys. Express **5**, 061102 (2012).
[2] H. J. Kim, U. Kim, T. H. Kim, J. Kim, H. M. Kim, B. G. Jeon, W. J. Lee, H. S. Mun, K. T. Hong, J. Yu, K. Char, and K. H. Kim, Phys. Rev. B **86**, 165205 (2012).
[3] X. Luo, Y. S. Oh, A. Sirenko, P. Gao, T. A. Tyson, K. Char, and S. W. Cheong, Appl. Phys. Lett. **100**, 172112 (2012).
[4] A. Prakash, P. Xu, A. Faghaninia, S. Shukla, J. W. Ager III, C. S. Lo, and B. Jalan, Nat. Commun. **8**, 15167 (2017).
[5] S. James Allen, S. Raghavan, T. Schumann, K. M. Law, and S. Stemmer, Appl. Phys. Lett. **108**, 252107 (2016).
[6] C. A. Niedermeier, S. Rhode, K. Ide, H. Hiramatsu, H. Hosono, T. Kamiya, and M. A. Moram, Phys. Rev. B **95**, 161202 (2017).
[7] D. J. Singh, Q. Xu, and K. P. Ong, Appl. Phys. Lett. **104**, 011910 (2014).
[8] K. Krishnaswamy, B. Himmetoglu, Y. Kang, A. Janotti, and C. G. Van de Walle, Phys. Rev. B **95**, 205202 (2017).
[9] D. O. Scanlon, Phys. Rev. B **87**, 161201 (2013).
[10] E. McCalla, D. Phelan, M. J. Krogstad, B. Dabrowski, and C. Leighton, Phys. Rev. Mater. **2**, 084601 (2018).
[11] K. Ganguly, P. Ambwani, P. Xu, J. S. Jeong, K. A. Mkhoyan, C. Leighton, and B. Jalan, APL Mater. **3**, 062509 (2015).
[12] J. Shin, Y. M. Kim, Y. Kim, C. Park, and K. Char, Appl. Phys. Lett. **109**, 262102 (2016).
[13] S. Raghavan, T. Schumann, H. Kim, J. Y. Zhang, T. A. Cain, and S. Stemmer, APL Mater. **4**, 016106 (2016).
[14] H. Paik, Z. Chen, E. Lochocki, A. Seidner H., A. Verma, N. Tanen, J. Park, M. Uchida, S. Shang, B. C. Zhou, M. Brützam, R. Uecker, Z. K. Liu, D. Jena, K. M. Shen, D. A. Muller, and D. G. Schlom, APL Mater. **5**, 116107 (2017).
[15] D. Yoon, S. Yu, and J. Son, NPG Asia Mater. **10**, 363 (2018).
[16] Z. Lebens-Higgins, D. O. Scanlon, H. Paik, S. Sallis, Y. Nie, M. Uchida, N. F. Quackenbush, M. J. Wahila, G. E. Sterbinsky, D. A. Arena, J. C. Woicik, D. G. Schlom, and L. F. J. Piper, Phys. Rev. Lett. **116**, 027602 (2016).
[17] H. Mizoguchi, P. Chen, P. Boolchand, V. Ksenofontov, C. Felser, P. W. Barnes, and P. M. Woodward, Chem. Mater. **25**, 3858 (2013).
[18] P. V. Wadekar, J. Alaria, M. O'Sullivan, N. L. O. Flack, T. D. Manning, L. J. Phillips, K. Durose, O. Lozano, S. Lucas, J. B. Claridge, and M. J. Rosseinsky, Appl. Phys. Lett. **105**, 052104 (2014).
[19] H. J. Kim, J. Kim, T. H. Kim, W. J. Lee, B. G. Jeon, J. Y. Park, W. S. Choi, D. W. Jeong, S. H. Lee, J. Yu, T. W. Noh, and K. H. Kim, Phys. Rev. B **88**, 125204 (2013).
[20] K. Ganguly, A. Prakash, B. Jalan, and C. Leighton, APL Mater. **5**, 056102 (2017).
[21] U. Kim, C. Park, T. Ha, R. Kim, H. S. Mun, H. M. Kim, H. J. Kim, T. H. Kim, N. Kim, J. Yu, K. H. Kim, J. H. Kim, and K. Char, APL Mater. **2**, 056107 (2014).

[22] H. Yun, K. Ganguly, W. Postiglione, B. Jalan, C. Leighton, K. A. Mkhoyan, and J. S. Jeong, Sci. Rep. **8**, 10245 (2018).

[23] W. Y. Wang, Y. L. Tang, Y. L. Zhu, J. Suriyaprakash, Y. B. Xu, Y. Liu, B. Gao, S. W. Cheong, and X. L. Ma, Sci. Rep. **5**, 16097 (2015).

[24] C. Park, U. Kim, C. J. Ju, J. S. Park, Y. M. Kim, and K. Char, Appl. Phys. Lett. **105**, 203503 (2014).

[25] Y. M. Kim, C. Park, U. Kim, C. Ju, and K. Char, Appl. Phys. Express **9**, 011201 (2016).

[26] K. Fujiwara, K. Nishihara, J. Shiogai, and A. Tsukazaki, AIP Adv. **6**, 085014 (2016).

[27] U. Kim, C. Park, T. Ha, Y. M. Kim, N. Kim, C. Ju, J. Park, J. Yu, J. H. Kim, and K. Char, APL Mater. **3**, 036101 (2015).

[28] J. Yue, A. Prakash, M. C. Robbins, S. J. Koester, and B. Jalan, ACS Appl. Mater. Interfaces **10**, 21061 (2018).

[29] S. Heo, D. Yoon, S. Yu, J. Son, and H. Myung Jang, J. Mater. Chem. C **5**, 11763 (2017).

[30] U. Kim, C. Park, Y. M. Kim, J. Shin, and K. Char, APL Mater. **4**, 071102 (2016).

[31] Y. Kim, Y. M. Kim, J. Shin, and K. Char, APL Mater. **6**, 096104 (2018).

[32] S. Z. Bisri, S. Shimizu, M. Nakano, and Y. Iwasa, Adv. Mater. **29**, 1607054 (2017).

[33] S. H. Kim, K. Hong, W. Xie, K. H. Lee, S. Zhang, T. P. Lodge, and C. D. Frisbie, Adv. Mater. **25**, 1822 (2013).

[34] K. H. Lee, M. S. Kang, S. Zhang, Y. Gu, T. P. Lodge, and C. D. Frisbie, Adv. Mater. **24**, 4457 (2012).

[35] H. Yuan, H. Shimotani, A. Tsukazaki, A. Ohtomo, M. Kawasaki, and Y. Iwasa, Adv. Funct. Mater. **19**, 1046 (2009).

[36] M. Nakano, K. Shibuya, D. Okuyama, T. Hatano, S. Ono, M. Kawasaki, Y. Iwasa, and Y. Tokura, Nature (London) **487**, 459 (2012).

[37] R. Scherwitzl, P. Zubko, I. G. Lezama, S. Ono, A. F. Morpurgo, G. Catalan, and J. M. Triscone, Adv. Mater. **22**, 5517 (2010).

[38] K. Ueno, S. Nakamura, H. Shimotani, A. Ohtomo, N. Kimura, T. Nojima, H. Aoki, Y. Iwasa, and M. Kawasaki, Nat. Mater. **7**, 855 (2008).

[39] J. T. Ye, Y. J. Zhang, R. Akashi, M. S. Bahramy, R. Arita, and Y. Iwasa, Science **338**, 1193 (2012).

[40] X. Leng, J. Garcia-Barriocanal, S. Bose, Y. Lee, and A. M. Goldman, Phys. Rev. Lett. **107**, 027001 (2011).

[41] N. Lu, P. Zhang, Q. Zhang, R. Qiao, Q. He, H. B. Li, Y. Wang, J. Guo, D. Zhang, Z. Duan, Z. Li, M. Wang, S. Yang, M. Yan, E. Arenholz, S. Zhou, W. Yang, L. Gu, C. W. Nan, J. Wu, Y. Tokura, and P. Yu, Nature (London) **546**, 124 (2017).

[42] J. Walter, T. Charlton, H. Ambaye, M. R. Fitzsimmons, P. P. Orth, R. M. Fernandes, and C. Leighton, Phys. Rev. Mater. **2**, 111406 (2018).

[43] H. T. Yi, B. Gao, W. Xie, S. W. Cheong, and V. Podzorov, Sci. Rep. **4**, 6604 (2014).

[44] B. Cui, C. Song, G. Wang, Y. Yan, J. Peng, J. Miao, H. Mao, F. Li, C. Chen, F. Zeng, and F. Pan, Adv. Funct. Mater. **24**, 7233 (2014).

[45] K. Fujiwara, K. Nishihara, J. Shiogai, and A. Tsukazaki, Appl. Phys. Lett. **110**, 203503 (2017).

[46] C. Leighton, Nat. Mater. **18**, 13 (2019).

[47] J. Walter, H. Wang, B. Luo, C. D. Frisbie, and C. Leighton, ACS Nano **10**, 7799 (2016).

[48] M. Nakano, D. Okuyama, K. Shibuya, M. Mizumaki, H. Ohsumi, M. Yoshida, M. Takata, M. Kawasaki, Y. Tokura, T. Arima, and Y. Iwasa, Adv. Electron. Mater. **1**, 1500093 (2015).

[49] J. Jeong, N. Aetukuri, T. Graf, T. D. Schladt, M. G. Samant, and S. S. P. Parkin, Science **339**, 1402 (2013).

[50] M. Li, W. Han, X. Jiang, J. Jeong, M. G. Samant, and S. S. P. Parkin, Nano Lett. **13**, 4675 (2013).

[51] T. D. Schladt, T. Graf, N. B. Aetukuri, M. Li, A. Fantini, X. Jiang, M. G. Samant, and S. S. P. Parkin, ACS Nano **7**, 8074 (2013).

[52] D. Okuyama, M. Nakano, S. Takeshita, H. Ohsumi, S. Tardif, K. Shibuya, T. Hatano, H. Yumoto, T. Koyama, H. Ohashi, M. Takata, M. Kawasaki, T. Arima, Y. Tokura, and Y. Iwasa, Appl. Phys. Lett. **104**, 023507 (2014).

[53] J. Walter, G. Yu, B. Yu, A. Grutter, B. Kirby, J. Borchers, Z. Zhang, H. Zhou, T. Birol, M. Greven, and C. Leighton, Phys. Rev. Mater. **1**, 071403 (2017).

[54] Y. Dong, H. Xu, Z. Luo, H. Zhou, D. D. Fong, W. Wu, and C. Gao, APL Mater. **5**, 051101 (2017).

[55] A. M. Perez-Muñoz, P. Schio, R. Poloni, A. Fernandez-Martinez, A. Rivera-Calzada, J. C. Cezar, E. Salas-Colera, G. R. Castro, J. Kinney, C. Leon, J. Santamaria, J. Garcia-Barriocanal, and A. M. Goldman, Proc. Natl. Acad. Sci. USA **114**, 215 (2017).

[56] S. Bubel, A. J. Hauser, A. M. Glaudell, T. E. Mates, S. Stemmer, and M. L. Chabinyc, Appl. Phys. Lett. **106**, 122102 (2015).

[57] X. Leng, J. Pereiro, J. Strle, G. Dubuis, A. T. Bollinger, A. Gozar, J. Wu, N. Litombe, C. Panagopoulos, D. Pavuna, and I. Božović, npj Quantum Mater. **2**, 35 (2017).

[58] M. Wang, S. Shen, J. Ni, N. Lu, Z. Li, H. B. Li, S. Yang, T. Chen, J. Guo, Y. Wang, H. Xiang, and P. Yu, Adv. Mater. **29**, 1703628 (2017).

[59] M. A. Hope, K. J. Griffith, B. Cui, F. Gao, S. E. Dutton, S. S. P. Parkin, and C. P. Grey, J. Am. Chem. Soc. **140**, 16685 (2018).

[60] H. Ji, J. Wei, and D. Natelson, Nano Lett. **12**, 2988 (2012).

[61] W. M. Postiglione, K. Ganguly, H. Yun, L. Borgeson, J. S. Jeong, K. A. Mkhoyan, B. Jalan, and C. Leighton (unpublished).

[62] See Supplemental Material at http://link.aps.org/supplemental/10.1103/PhysRevMaterials.3.075001 for additional information on assessing x-ray beam damage in *operando* SXRD measurements, resistance change after ion gel gating, calculations of induced electron profile, and the crossover from Mott to Efros-Shklovskii hopping.

[63] A. Prakash, P. Xu, X. Wu, G. Haugstad, X. Wang, and B. Jalan, J. Mater. Chem. C **5**, 5730 (2017).

[64] M. Wang, X. Sui, Y. Wang, Y. H. Juan, Y. Lyu, H. Peng, T. Huang, S. Shen, C. Guo, J. Zhang, Z. Li, H. B. Li, N. Lu, A. T. N'Diaye, E. Arenholz, S. Zhou, Q. He, Y. H. Chu, W. Duan, and P. Yu, Adv. Mater. **31**, 1900458 (2019).

[65] A. Spinelli, M. A. Torija, C. Liu, C. Jan, and C. Leighton, Phys. Rev. B **81**, 155110 (2010).

[66] W. J. Lee, H. J. Kim, E. Sohn, H. M. Kim, T. H. Kim, K. Char, J. H. Kim, and K. H. Kim, Phys. Status Solidi A **212**, 1487 (2015).

[67] R. A. De Souza, Adv. Funct. Mater. **25**, 6326 (2015).

[68] L. R. Thoutam, J. Yue, A. Prakash, T. Wang, K. E. Elangovan, and B. Jalan, ACS Appl. Mater. Interfaces **11**, 7666 (2019).

[69] S. Jo, D. Costanzo, H. Berger, and A. F. Morpurgo, Nano Lett. **15**, 1197 (2015).

[70] H. Ohno, *Electrochemical Aspects of Ionic Liquids* (John Wiley & Sons, New Jersey, 2005).
[71] S. Zeng, W. Lü, Z. Huang, Z. Liu, K. Han, K. Gopinadhan, C. Li, R. Guo, W. Zhou, H. H. Ma, L. Jian, T. Venkatesan, and Ariando, ACS Nano **10**, 4532 (2016).
[72] R. L. Petritz, Phys. Rev. **110**, 1254 (1958).
[73] B. Arnaudov, T. Paskova, S. Evtimova, E. Valcheva, M. Heuken, and B. Monemar, Phys. Rev. B **67**, 045314 (2003).
[74] K. V. Reich, M. Schecter, and B. I. Shklovskii, Phys. Rev. B **91**, 115303 (2015).
[75] J. Suñé, P. Olivo, and B. Riccó, J. Appl. Phys. **70**, 337 (1991).
[76] J. Suñé, P. Olivo, and B. Riccó, IEEE Trans. Electron Devices **39**, 1732 (1992).
[77] H. Wang, K. Ganguly, A. Prakash, K. V. Reich, J. Walter, B. Jalan, B. I. Shklovskii, and C. Leighton (unpublished).
[78] A. G. Zabrodskii, Philos. Mag. B **81**, 1131 (2001).
[79] B. I. Shklovskii and A. L. Efros, *Electronic Properties of Doped Semiconductors*, Springer Series in Solid-State Sciences (Springer, Berlin, 1984).
[80] N. Mott, *Metal-Insulator Transitions* (CRC Press, London, 1990).
[81] P. A. Lee and T. V. Ramakrishnan, Rev. Mod. Phys. **57**, 287 (1985).
[82] There is some evidence in Fig. 6(a) and Fig. S4 of deviations from ES VRH towards some strong T dependence (i.e., $m > 0.5$) at low T. Low T studies are required, but there are known effects capable of this, e.g., I. Terry, T. Penney, S. von Molnár, and P. Becla, Phys. Rev. Lett. **69**, 1800 (1992).
[83] S. Wang, M. Ha, M. Manno, C. Daniel Frisbie, and C. Leighton, Nat. Commun. **3**, 1210 (2012).
[84] Y. Zhang, P. Dai, M. Levy, and M. P. Sarachik, in *Hopping Related Phenomena* (World Scientific, Singapore, 1990), pp. 85–92.